

# Fast X-ray powder diffraction on I11 at Diamond

Stephen P. Thompson,<sup>a</sup> Julia E. Parker,<sup>a</sup> Julien Marchal,<sup>a</sup> Jonathan Potter,<sup>a</sup> Adrian Birt,<sup>a</sup> Fajin Yuan,<sup>a</sup> Richard D. Fearn,<sup>a</sup> Alistair R. Lennie,<sup>a</sup> Steven R. Street<sup>a</sup> and Chiu C. Tang<sup>a,b\*</sup>

<sup>a</sup>Diamond Light Source, Diamond House, Harwell Science and Innovation Campus, Didcot, Oxfordshire OX11 0DE, UK, and <sup>b</sup>School of Materials, The University of Manchester, Manchester M13 9PL, UK. E-mail: chiu.tang@diamond.ac.uk

The commissioning and performance characterization of a position-sensitive detector designed for fast X-ray powder diffraction experiments on beamline I11 at Diamond Light Source are described. The detecting elements comprise 18 detector-readout modules of MYTHEN-II silicon strip technology tiled to provide 90° coverage in  $2\theta$ . The modules are located in a rigid housing custom designed at Diamond with control of the device fully integrated into the beamline data acquisition environment. The detector is mounted on the I11 three-circle powder diffractometer to provide an intrinsic resolution of  $\Delta 2\theta \simeq 0.004^\circ$ . The results of commissioning and performance measurements using reference samples (Si and AgI) are presented, along with new results from scientific experiments selected to demonstrate the suitability of this facility for powder diffraction experiments where conventional angle scanning is too slow to capture rapid structural changes. The real-time dehydrogenation of  $\text{MgH}_2$ , a potential hydrogen storage compound, is investigated along with ultrafast high-throughput measurements to determine the crystallite quality of different samples of the metastable carbonate phase vaterite ( $\text{CaCO}_3$ ) precipitated and stabilized in the presence of amino acid molecules in a biomimetic synthesis process.

**Keywords:** *in situ* synchrotron powder diffraction; fast position-sensitive detector.

## 1. Introduction

Synchrotron X-ray powder diffraction (SXP) beamlines equipped with single, angle-scanning, point detectors have proved to be very successful in obtaining high-resolution data with  $\Delta d/d$  typically  $\sim 10^{-4}$ – $10^{-5}$  (e.g. Cox *et al.*, 1983; Hastings *et al.*, 1984; Cernik *et al.*, 1990; Toraya *et al.*, 1996). However, data collection times for these instruments are of the order of a few hours per pattern and are limited by the incident X-ray flux, requiring relatively long count times per point in order to achieve good statistics, and limited by the time necessary to physically perform a series of angle-resolved point collections over a given angular range. Although significant improvements have been achieved at high-brightness third-generation synchrotron sources by the development of multiple analysing crystal systems (Fitch, 1996, 2004; Hodeau *et al.*, 1998; Gozzo *et al.*, 2004; Lee *et al.*, 2008; Wang *et al.*, 2008; Thompson *et al.*, 2009), the measurement of whole powder patterns can still take somewhere between a few minutes and a few tens of minutes, even when continuous scanning, over step scanning, is routinely employed. Further improvements in speed may yet be possible, but will remain limited by the mechanics of

motion for the diffractometer and the need for good counting statistics.

As an alternative, the use of wide-angle detecting devices, able to simultaneously record entire patterns without scanning, can considerably speed up data collection. Although resolution and dynamic range (signal-to-background contrast) may sometimes be compromised, such detectors are essential for investigating material systems whose structures evolve over timescales that are shorter than the fastest achievable angle-scanning times, particularly under non-ambient conditions. In addition to time-resolved experiments, the ability to measure large numbers of different samples within a relatively short time is an important attraction too, offering the prospect of high-volume high-throughput studies on samples with subtle compositional or structural variation.

Pioneering position-sensitive detectors (PSDs) built for applications requiring fast measurements were developed in the early years of SXP (see, for example, the review by Hasegawa *et al.*, 1986). Driven by scientific objectives and advances in electronics, various fast detection systems (linear PSD and area detectors) have been developed. Flat and curved (in  $2\theta$ ) image plates have been used successfully on

beamlines for many years (e.g. Norby, 1997; Nishibori *et al.*, 2001; Martorana *et al.*, 2003; Lennie *et al.*, 2007). However, temporal resolution is largely limited by the readout and erase times following each exposure, typically a few minutes per pattern. CCD-based pixel detectors, consisting of an input phosphor screen, image intensifier, optical lens coupling and camera, have been developed and applied at the ESRF (Svensson *et al.*, 1997; Kvik, 2003) giving a collection rate of 100 ms per frame for in excess of 100 frames (Kvik, 2003). Wide-angle multi-wire gas proportional detectors were originally developed at the NSLS and used on beamline X7A (Smith, 1991), with a similar device being developed at the Daresbury SRS and used on beamline MPW6.2 (Cernik *et al.*, 2004; Tang *et al.*, 2004). The time resolution of these devices is on a scale of milliseconds to sub-seconds per pattern, assuming there is no X-ray flux limitation. However, operationally the extrapolation of angular positions limits their usefulness for routine detailed structure determinations, *i.e.* atomic positions, temperature factors and site occupancy. Recently, at the Swiss Light Source, Schmitt *et al.* (2003) have developed a PSD based on MYTHEN (Microstrip sYstem for Time-rEsolved experimeNts) silicon microstrip technology, which was first used on the X04SA materials science beamline (Gozzo *et al.*, 2004). This device, which has since been upgraded to include MYTHEN-II modules (Bergamaschi *et al.*, 2009; Gozzo *et al.*, 2010), presents a wide-angle, pseudo-curved, detecting surface built up from linear MYTHEN modules tiled at a sufficient distance from the sample to minimize parallax effects over each module. Frame rates of up to 100 Hz can be achieved for a 120° detector assembled from 24 MYTHEN modules (Bergamaschi *et al.*, 2010). Another MYTHEN-II PSD of 80° aperture has been recently commissioned on the powder diffraction beamline at the Australian Synchrotron (Wallwork *et al.*, 2007).

Although the above summary is not an exhaustive review it does highlight the trend in development at synchrotron facilities, where the benefits and new possibilities for the study of polycrystalline materials are clearly recognized. Each detector system has its own inherent advantages and disadvantages and its suitability and choice for any given application, or beamline, depends on many factors including the scientific objectives, availability of technology, and cost. In designing and constructing a powder beamline at a new synchrotron source, the unique opportunity arises to specify a detection system whose key performance criteria are driven mainly by scientific objectives, rather than having to adapt to pre-existing optics, X-ray beam or diffractometer hardware. In this paper we therefore present the commissioning and performance characteristics of a new PSD on beamline I11 at the Diamond Light Source using MYTHEN-II silicon microstrip detection technology, specifically aimed at the fast recording of wide-angle powder diffraction data with sufficient statistical quality and resolution (*i.e.*  $\Delta d/d \simeq 10^{-3}$ – $10^{-4}$ ) to allow Rietveld refinement methods to be used in its analysis. Integral to the original beamline design, and intended to complement the high-resolution angle-scanning capability of the beamline (Thompson *et al.*, 2009), this new

detector comprises 18 linear modules arranged in a 90° arc concentric to the  $2\theta$  circle.

Commissioning results using standard Si powder and the  $\beta/\gamma$ - $\alpha$  phase transition of silver iodide are presented. To demonstrate its use in a variety of powder experiments, results are presented from two different experiments where the use of a PSD offers distinct advantages. Firstly, data from a time-resolved study of the collapse of tetragonal structure in MgH<sub>2</sub> at elevated temperatures are presented. Although the structural details of this compound have been known for several decades (Zachariassen *et al.*, 1963), this and related compounds are currently the subject of intense interest as base materials in the development of future hydrogen storage technology (Schlapbach & Züttel, 2001). Secondly, results are described from an ultra-fast high-throughput experiment to study the use of amino acids in the production and phase stabilization of vaterite, a metastable anhydrous CaCO<sub>3</sub> phase, *via* biomimetic synthesis. The structure of vaterite is still the subject of some debate since its occurrence in nature is rare, often forming poor crystallites.

## 2. Design and technical considerations

### 2.1. Choice of detection technology

Based on scientific requirements and the X-ray beam characteristics of the undulator-sourced I11 powder beamline (Thompson *et al.*, 2009) at the Diamond third-generation synchrotron, the specifications for a PSD capable of providing maximum flexibility and performance over a range of experimental conditions were identified from the beginning of the beamline design (Tang *et al.*, 2007). Essentially, the choice is dictated by the interplay between the need for good statistics (*i.e.* exposure time), sensitivity (*i.e.* low noise/background, wide dynamic range) and frame rate (*i.e.* readout time). Associated with this last criterion is duration, *i.e.* the length of time, or maximum number of frames, for which the frame rate can be maintained. It was recognized early on that a photon-counting device based on Si strip detection would satisfy most of the requirements laid out for I11, as well as providing a device that was straightforward to maintain and operate. The decision was therefore made to construct a modular PSD using MYTHEN-II technology. The I11 PSD design requirements and MYTHEN-II performance specifications are outlined in Table 1.

The sensors incorporated into each MYTHEN-II module are 300  $\mu\text{m}$ -thick Si p-n junction microstrips. The microstrips consist of depleted high-resistivity n-doped silicon wafers segmented on one side by optical lithography into a number of pixellated strips, each behaving like a reverse-biased diode. Each module, 8 mm (width)  $\times$  62 mm (length), consists of 1280 strips of 50  $\mu\text{m}$ -pitch silicon sensor. Electron-hole pairs are created by the impinging X-ray photons and separated by a bias voltage applied to the junction. On average, 3.62 eV are needed to create one electron-hole pair. Owing to the absorption cross section of Si, the detector efficiency is energy dependent and decreases from  $\sim 100\%$  at 7 keV to  $\sim 15\%$  at

**Table 1**  
Key specifications for I11 PSD and MYTHEN-II modules.

I11 PSD requirements	
Angular coverage ( $2\theta$ )	90°
Energy range	6–20 keV
Efficiency at 12 keV	70% or better
Angular resolution ( $\Delta 2\theta$ )	0.005° or better
Frame rate per whole pattern	20 Hz
Number of frames	500
Total weight (including housing)	35 kg
MYTHEN-II modules	
Number of modules for 90°	18
Strip pitch	50 $\mu\text{m}$
Channels per module	1280
Sample–sensor distance	760 mm [ $\sim 0.004^\circ$ (intrinsic resolution)]
Energy range	6–20 keV
Efficiency at 12 keV	73%
Frame rate (single module)	100–900 Hz†

† Depending on bit depth (Bergamaschi *et al.*, 2010).

25 keV (Gozzo *et al.*, 2004). The detector operates in single-photon-counting mode such that each X-ray generating a charge above a given threshold is counted. The threshold is set to half the X-ray photon energy to avoid double counts or count loss related to charge-sharing effects in highly segmented silicon detectors (Marchal, 2010a,b).

Readout is *via* a 128-channel application-specific integrated circuit (ASIC) directly wire bonded to the sensor, with each channel being independent of the others, providing for fast readout of scattered data. The readout chip is designed to have noise levels several times lower than the threshold to avoid noise counts and low threshold fluctuations. The maximum frame rate is determined by the number of modules to be read out and/or the number of bits used to transfer data (see §3). For each module a threshold dispersion of approximately 140 eV FWHM (full width at half-maximum) was measured after equalization of the 6-bit adjustment detection thresholds. A more detailed technical account of the MYTHEN modules is given by Schmitt *et al.* (2003) and Bergamaschi *et al.* (2009, 2010); here we focus only on the I11-specific technical specifications, mechanical design, installation and commissioning characterization measurements.

### 3. PSD design, intrinsic resolution and frame rate

The mechanical housing and mounting arrangements for the PSD modules were designed at Diamond. The body is made from a C250 aluminium cast machined tooling plate, manufactured from a 5083 type alloy (ThyssenKrupp Materials UK). This was chosen for its high thermal stability (coefficient of thermal expansion =  $23.3 \times 10^{-6} \text{ K}^{-1}$ ) and ease of machining (very low stress) while still retaining high mechanical strength. The design includes integral cross member structures machined into its body to provide mechanical rigidity, preventing any distortion of the module tiling and hence to the detecting surface as a whole should the housing be evacuated to reduce air scatter. Alternatively, the

design also allows for the whole housing to be filled with helium gas. The housing is designed such that 18 modules are populated in a 90° arc around the sample position as indicated in Fig. 1(a), with the whole ensemble mounted on the diffractometer’s  $\delta$ -circle (Fig. 1b). Note that the  $\delta$  angle is the diffraction Bragg angle and is therefore referred to as  $2\theta$  when discussing diffraction results below. In the absence of collimation, the intrinsic resolution,  $\Delta 2\theta$ , of a pixellated detector such as this is governed by the sample-to-detector distance,  $L$ , and the Si microstrip pitch,  $p$ , which are related *via* simple geometry,

$$\Delta 2\theta = \arctan(p/L). \quad (1)$$

However, in practice this is made worse by the sample diameter,  $t$ , as in Debye–Scherrer capillary geometry, such that

$$\Delta 2\theta_{\text{cap}} = 2 \arctan\left(\frac{p+t}{2L}\right). \quad (2)$$

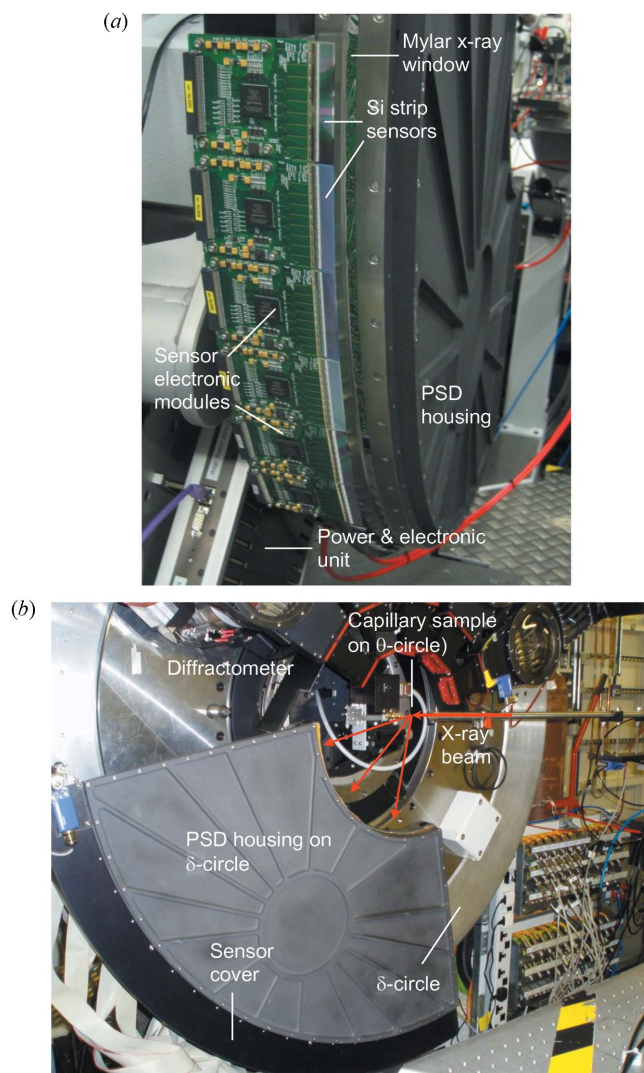


**Figure 1**  
Photographs of the PSD during installation: (a) showing the assembly of six modules, (b) complete assembly ready for commissioning.

In order to meet the specified resolution requirement of  $0.005^\circ$ , or better, the modules are located at a distance of 760 mm from the sample position. Owing to its modular nature, tiling the sensors leaves a small gap of  $\sim 1$  mm between adjacent modules which can be accounted for, in all but the fastest of experiments, by collecting datasets at two detector positions approximately  $0.25^\circ$  apart in  $2\theta$  and merging these to form a single continuous data file. The measured width of a Bragg peak will be a convolution of the microstrip size, the intrinsic point spread function, sample size (capillary diameter), capillary misalignment (wobble) and the axial beam divergence (Finger *et al.*, 1994) arising from the detector lateral width (see Bergamaschi *et al.*, 2010). The point spread function arises from the Si strip pixel pitch and has an inverse dependency on the detector threshold and a weak dependency on X-ray energy, but is typically  $\sim 1$  mdeg in  $2\theta$  (Bergamaschi *et al.*, 2008), while the axial contribution is proportional to  $\cot(\theta)$ , which for the 8 mm axial dimension of the MYTHEN strip can be considered negligible for  $2\theta > 10^\circ$ . The largest contribution to measured peak widths is therefore governed by the sample size and capillary misalignment. For powder patterns with lower angle peaks, the asymmetry correction can be performed using the 'simple' or 'full' axial model (Cheary & Coelho, 1998*a,b*) or the Finger *et al.* (1994) method which are available in *TOPAS*. The 18 detector modules are connected by 80 cm-long ribbon cables to a control board at the back of the housing. This includes an embedded Linux system and transfers image data to the beamline server using TCP/IP protocol *via* a client-server architecture.

#### 4. Hardware and data acquisition

Since the importance of providing a fast PSD capability for I11 was identified early in the beamline's technical design, provision for mounting such a device was incorporated into the diffractometer (custom made by Newport). Consequently the diffractometer comprises three concentric circles,  $\theta$ ,  $2\theta$  and  $\delta$ , housing the sample stage, high-resolution multi-analysing crystals system and PSD, respectively (Fig. 1*b*). The diffractometer's design and mechanical performance specifications are given by Thompson *et al.* (2009) along with details of the X-ray beam characteristics of the beamline. The  $\delta$ -circle is designed to hold up to 40 kg, making it capable of carrying the large PSD. The usual means of sample mounting is *via* magnetic holders which engage on a precision-engineered spinner pre-aligned with the diffractometer's centre of rotation (see Parker *et al.*, 2011). Alignment of the capillary in the magnetic holder can be done using an offline alignment jig with an accuracy of  $\pm 25 \mu\text{m}$ . The offline alignment offers distinct advantages for high-throughput experiments. The spin frequency is selected in software and may be varied from 90 to 4640 r.p.m. to suit the acquisition time. For experiments requiring traditional spinner geometry, a goniometer with *XY* translation and two arcs for alignment can be mounted on the  $\theta$ -circle.

To provide flexibility in designing and configuring experiments, control of the MYTHEN hardware *via* its dedicated

controller is integrated with Diamond's Generic Data Acquisition system (GDA, <http://www.opengda.org/OpenGDA/Documentation.html>), which is the common user interface implemented throughout Diamond. It comprises a graphical user interface client that allows commands and scripts to be entered and a server that controls specific beamline components through an EPICS interface layer. The GDA server communicates with the MYTHEN controller *via* a command-line MYTHEN client. This command-line client implements the necessary communication protocols and methods to enable the remote access and control of the detector.

The raw data received from the detector are saved to the beamline storage server and automatically processed by GDA software for bad-channel removal, flat-field correction and channel number to  $2\theta$  angle conversion. The corrected file is then passed back to the GDA client for display. In this mode, high-quality patterns suitable for structural refinement can be collected at frame rates of 7 Hz. Depending on the experimental requirements, the merging of two frames collected at two different PSD positions to bridge the gaps between individual modules, or the summation of multiple frames collected at a fixed detector position, can be carried out either automatically by GDA, immediately following data collection and raw data processing, or offline at a later stage. Summation of data collected at two different  $\delta$  positions involves the binning of each dataset onto a regular  $2\theta$  array, followed by direct summation of the intensities at each point and calculation of the resulting e.s.d. For those portions of the  $2\theta$  array where only one module is contributing (*i.e.* in the gaps between modules), the intensity from that module is counted twice to avoid intensity dips in the final summed data.

Simple intuitive software commands have been developed to provide a syntax that supports both single and multiple frames of data collection and user written scripts. The MYTHEN detector object can also be used with other GDA scan commands to allow the automated triggering of data collection based on a secondary condition such as a range of states reached within a sample cell. This can be achieved either by scanning the device state and collecting any number of datasets at regular intervals, or by the sending of a TTL pulse to the PSD from the cell itself once a given state is reached. To limit the exposure of radiation-sensitive samples to X-rays, a fast shutter is embedded as a permanent beamline component upstream of the diffractometer and provides GDA with a fine control for the X-ray exposure time to within  $\sim 5$  ms. The shutter is opened automatically when data collection is triggered and closed once the counting period has expired.

#### 5. Commissioning and calibration

In order to deliver the PSD as a fully operational user facility, several commissioning steps and calibration measurements were carried out in order to test its function and performance. These divided between operations necessary to the functioning of the MYTHEN sensors and readout electronics for X-ray detection and those required in order to deliver the

whole device as a functioning PSD on I11. The MYTHEN-specific steps are discussed in greater detail by Bergamaschi *et al.* (2010).

### 5.1. MYTHEN modules: threshold trimming, energy calibration and bad channels

Each readout channel includes a comparator circuit whose threshold voltage level must be defined for each module. Channel-to-channel variations must be corrected for to ensure that the overall energy resolution of the detector is consistent. This trimming is performed using an internal 6-bit digital-to-analogue converter (DAC), which determines an offset to be applied to the comparator threshold voltage. During commissioning the thresholds were trimmed using the background electronic noise, which in the absence of X-ray beam was assumed to be uniform across each module. Each channel was trimmed for gain/shaping time settings of ‘fast’, ‘standard’ and ‘high’ to give optimal performance at high photon rates and high energies (fast), normal intermediate photon rates and energies (standard), and long acquisition times at low energies (high).

Since the detection energy threshold is determined by the discriminator threshold voltage, energy calibration is necessary in order to produce the conversion between detection energy threshold and discriminator threshold DAC units. Energy calibration is thus required for each of the three gain settings and is obtained by illuminating the whole PSD with monochromatic X-rays and acquiring data while scanning the discriminator DAC values. Scattering from glass was used to produce monochromatic illumination over all 18 modules. An automated procedure based on the method described by Bergamaschi *et al.* (2009) was used to fit the S-curves at each energy with an error function plus a linear term, determine the S-curve inflection points and to perform a linear fit to these as a function of energy. Fig. 2(a) shows the number of X-ray counts as a function of threshold energy (S-curve) after conversion of the DAC values into X-ray keV units. The overall energy resolution of a module can be measured by differentiating the S-curve as shown in Fig. 2(b). A FWHM of  $\sim 2$  keV was achieved for all 18 modules. If required, this could be improved further by trimming the thresholds using X-rays rather than the background noise. Owing to the presence of a charge-sharing related low-energy tail added to the Gaussian X-ray energy distribution for each module, setting the threshold to more than half the X-ray energy will result in a loss of X-ray counts. However, experiments where sample fluorescence is strong can benefit from higher threshold settings, and better quality diffraction data can be obtained by setting the detection threshold such that it is  $\geq 3$  keV higher than any fluorescence line and  $\leq 3$  keV lower than the X-ray beam energy (Haverkamp & Wallwork, 2009).

A given channel is considered to be bad if it always produces zero counts (*i.e.* is a dead channel), or if it gives count rates three times higher or lower than the mean count rate over the detector when exposed to flat-field X-ray illumination (see §5.2). Bad channels can be due to a faulty wire

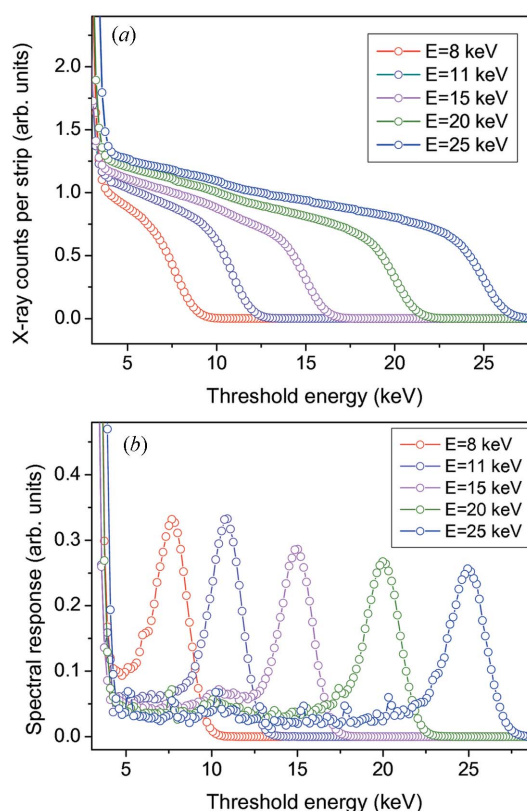


**Figure 2**

(a) S-curve data obtained during the energy calibration of one of the 18 modules. X-rays of 8, 11, 15, 20 and 25 keV scattered from a glass plate were used to calibrate the detector. (b) Differentiated S-curve data showing the overall energy resolution ( $\sim 2$  keV FWHM) of a MYTHEN module at 8, 11, 15, 20 and 25 keV.

bond connection or a noisy readout channel in the ASIC. These can arise during manufacture or can fail in operation and can be masked out during data acquisition. A bad channel list is thus produced from flat-field images using a low detection threshold. During commissioning, the number of bad channels over the 23040 total PSD channels was 3, 6 (see Fig. 3, top) and 37 for the fast, standard and high gain settings, respectively.

### 5.2. Detector commissioning: angular calibration and flat-field correction

Angular calibration is required to correct for differences in the positioning and arc of the linear modules within the PSD. This is done by scanning the whole detector across a well defined Bragg reflection of a Si reference powder sample (see §6.1 for sample details). For each angular position a fit is performed on the selected peak and its centre position calculated. The position of the peak centre as a function of detector angle is used to produce a set of geometrical factors for each module that correct for errors in the module-centre to diffractometer-centre distance and module tilt. These small geometrical errors are then automatically corrected for in GDA when converting channel number to  $2\theta$  value. Refinement of a full Si powder pattern was then used to determine the  $2\theta$  zero point of the whole detector.

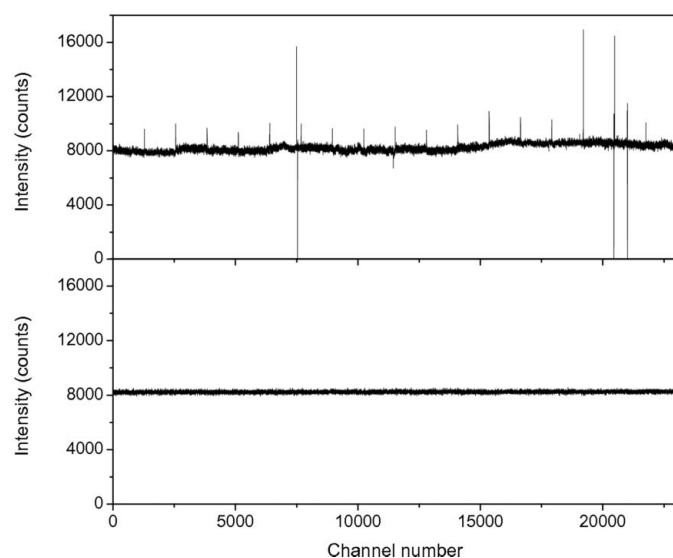


**Figure 3**  
Flat-field illumination on the PSD using scattered X-rays ( $E = 20$  keV) showing raw data with regular spikes from the edges of modules and the large spikes of the six bad channels (top), and flat-field- and dead-channel-corrected data (bottom).

Any non-uniformity in strip-to-strip response remaining after threshold trimming is eliminated by applying a flat-field correction. A flat field can be obtained in a manner similar to the angular correction, by scanning the detector through a well defined X-ray beam. For this, a glass capillary was located at the diffractometer centre and surrounded by an incomplete cylindrically shaped lead mask in which a small aperture is made to allow scattered X-rays to exit at a fixed scattering angle. The scattered beam was further defined by mounting a set of slits after the aperture to provide a  $\sim 1^\circ$  angular exposure at the detector. The PSD was then scanned through the scattered beam repeatedly, until 100000 counts were recorded on each pixel, to allow a set of averaged flat-field correction coefficients to be constructed. Fig. 3 shows flat-field data collected at 20 keV, with threshold set at 10 keV, before (top) and after correction (bottom). As can be seen in the figure, the flat-field correction corrects for the 10% higher counts produced by those strips located at the edges of the modules and any other differences in counting behaviour.

## 6. Experimental details

In commissioning and demonstrating the scientific capability of the I11 PSD, several measurements were performed and are detailed below. Ambient commissioning measurements on a NIST silicon reference powder were performed to gauge the data quality with differing acquisition times. These were then followed by time-resolved observations of the well known phase transition in silver iodide to demonstrate the suitability of the device for obtaining crystallographic details from an evolving system. Finally, building on these, two scientific experiments are presented that demonstrate its use in time-resolved studies and multi-sample ultra-fast high-throughput measurements.

### 6.1. Reference materials

Samples of silicon and silver iodide (AgI) were used to characterize the performance of the PSD. Powder samples of each were loaded into 0.5 mm (internal diameter) borosilicate glass capillaries and measurements made with the specimen placed on the pre-aligned sample spinner at the centre of the  $\theta$ -circle. Diffraction patterns from the high-quality Si powder sample [NIST SRM640c, faced-centred cubic,  $Fd\bar{3}m$ , with certified lattice parameter  $a_0 = 5.431195(9)$  Å at room temperature] were collected for different exposure times. The PSD powder patterns were analysed using *TOPAS (General Profile and Structure Analysis Software for Powder Diffraction Data, version 3.0, Bruker AXS GmbH)*.

The detector was positioned at  $5^\circ$  (first silicon strip) and then used to measure the phase transition of AgI. At room temperature and pressure, this compound exists in both a hexagonal (close-packed)  $\beta$ -phase (wurtzite structure) and a metastable cubic (close-packed)  $\gamma$ -phase (sphalerite structure). Published lattice parameters are  $a = 4.5800$ ,  $c = 7.494$  Å (space-group symmetry  $P6_3mc$ ) and  $a = 6.4991$  Å (space-group symmetry  $F43m$ ), respectively. Above 420 K it undergoes a crystalline transition to the  $\alpha$ -phase, which has a body-centred-cubic framework of I ions with the Ag cations distributed over a sub-lattice of interstitial sites ( $a = 5.048$  Å, space group  $Im\bar{3}m$ ). Details of the structures and phase transition are given by Merrill (1977) and Mellander *et al.* (1980). The sample was heated from 400 to 450 K at  $360$  K  $h^{-1}$  using an Oxford Cryostream Plus, with diffraction patterns recorded at a rate of 1 s per frame for 355 frames (with 0.35 s data processing time per frame).

### 6.2. MgH<sub>2</sub> hydrogen storage material

Hydrogen storage represents a significant challenge in developing viable hydrogen-powered vehicles and is possibly the most technologically demanding aspect of achieving a post-petroleum hydrogen-based economy. While high-pressure tanks have been used in several prototype cars, the required gas volume to be stored is high but the useful capacity is low, while safety concerns also call for alternative solutions. Light metal hydrides such as MgH<sub>2</sub> offer a possible solution to this problem (Schlapbach & Züttel, 2001) owing to their ability to absorb high quantities of hydrogen (7.6 mass% H for MgH<sub>2</sub>). There are, however, technical issues associated with MgH<sub>2</sub>, such as strong H–Mg bonding up to 700 K and slow H diffusion impeding the loading–unloading cycle; consequently much effort has been given to producing and/or treating similar related or alloyed compounds in order to reduce the diffusion path of H atoms (Jensen *et al.*, 2006, and references therein). Nevertheless, MgH<sub>2</sub> has the highest known storage capacity and gaining an understanding of the structural reorganization that occurs as hydrogen is removed from the lattice is important in realising a future high-capacity solid-phase portable storage material.

MgH<sub>2</sub> powder (Sigma Aldrich) was loaded and sealed in a 0.5 mm capillary in an argon-filled glove box and heated *in situ* using a Cyberstar hot air blower. The hot air blower was

mounted on a moveable (*XYZ*) table allowing it to be engaged or disengaged by horizontal translation of the table. The hot air blower temperature was set to 733 K, 773 K or 823 K and, once reached, the hot air blower was moved into position by GDA and PSD data collection initialized. At 733 K, datasets were collected for 1 s per exposure at two  $\delta$ -circle positions (12 and 12.25°) to bridge the module gaps, and then automatically summed, until dehydrogenation had occurred. Owing to the time taken to sum the data from two  $\delta$  positions, write three separate files, plot the data in GDA and move the  $\delta$  circle, this gave a time interval of approximately 6.5 s per frame. In order to increase the speed of data collection at 773 K or 823 K, where the reaction would be expected to proceed faster, exposures were collected for 2 s per frame each at fixed  $\delta = 12^\circ$ .

### 6.3. Ultra-fast high-throughput (u-HT) study of biomimetic vaterite

Calcium carbonate mineralization (both geological and biogenic) is of considerable interest for geochemists, material scientists, palaeontologists and biologists (Jacob *et al.*, 2008; Tang *et al.*, 2009). The anhydrous  $\text{CaCO}_3$  mineral phases calcite and aragonite are commonly found in rocks and organisms (*e.g.* corals, bivalves and gastropods) while the vaterite phase is rare owing to its higher solubility and tendency to convert to one of the more stable phases. Early publications (Meyer, 1960; Kamhi, 1963) report vaterite as having either an orthorhombic ( $a = 4.13$ ,  $b = 7.15$ ,  $c = 8.48$  Å, space group *Pbnm*) or hexagonal structure ( $a = 4.13$ ,  $c = 8.49$  Å, space group *P6<sub>3</sub>/mmc*), while a larger hexagonal unit cell (*P6<sub>3</sub>/mmc*,  $a = 7.16$ ,  $c = 16.98$  Å,  $Z = 12$ ) geometrically related to the smaller cell ( $a' = a/\sqrt{3}$ ,  $c' = c/2$ ) is also possible (Kamhi, 1963; Meyer, 1969). The actual crystal lattice of this rare phase is still uncertain, as discussed by Tang *et al.* (2009), who produced vaterite by the dehydration of a precursor ikaite ( $\text{CaCO}_3 \cdot 6\text{H}_2\text{O}$ ) phase. However, the crystal quality was too poor for structural analysis using high-resolution SXPD (nano-crystallites and strained) and LeBail refinements could be well fitted with both the smaller and larger hexagonal cells. The crystal details of vaterite are important to structurally 'connect' the vaterite–aragonite–calcite polymorph system and may provide a better understanding of the grand scheme of  $\text{CaCO}_3$  mineralization. In the current work a biomimetic synthesis method (described below) was used to produce a variety of samples containing differing proportions of the  $\text{CaCO}_3$  phases by varying the synthesis conditions. Phase content and crystal quality were then studied in a u-HT experiment using the PSD in combination with the beamline's automated robotic sample-changing facility (Parker *et al.*, 2011) in order to quickly determine which of the synthesis conditions produced the best vaterite crystals for further crystallographic study.

Although uncommon in nature, vaterite is also produced by organisms, both normally and under pathologic conditions (Lowenstam & Abbott, 1975; Spann *et al.*, 2010). Large macromolecules are known to be important in  $\text{CaCO}_3$

biomineralization in both the directing of morphological growth and the stabilization of the metastable aragonite/vaterite phases (see, for example, Barber, 1994; Aizenberg *et al.*, 1996, 2002; Mikkelsen *et al.*, 1997; Bezares *et al.*, 2008; Checa *et al.*, 2009). In a recent comparative study of synthetic and biogenic aragonite (Parker *et al.*, 2010), the hydrolysis of urea method (Wang *et al.*, 1999) was used to produce high-quality aragonite crystals. The urea protocol has therefore been modified (Thompson *et al.*, 2011) by adding  $\alpha$ -amino acids to the solution in which the carbonates precipitated. All the amino acids used in this study can exist in two chiral optical isomer forms (L- and D-) and carbonate precipitates were grown in the presence of each. Analytical-grade  $\text{CaCl}_2 \cdot \text{H}_2\text{O}$  (VWR International) and urea [ $(\text{NH}_2)_2\text{CO}$ , Fisher Scientific] were used to synthesize crystals of  $\text{CaCO}_3$  via direct precipitation in 50 ml deionized water by ageing solutions of  $\text{CaCl}_2$  ( $0.25 \text{ mol dm}^{-3}$ ) and urea ( $0.75 \text{ mol dm}^{-3}$ ) at 363 K for 20 h. The precipitates were removed by filtration, rinsed with distilled water, dried overnight at 363 K and stored in a desiccator. The procedure was repeated with 0.1, 0.2, 0.3 and 0.5 g of the various amino acids (Sigma Aldrich) added to give 2, 4, 6 and 10 g  $\text{L}^{-1}$  concentrations. The first indication that the modified urea process could stabilize vaterite came from examining precipitates formed in the presence of leucine [ $\text{HO}_2\text{CCH}(\text{NH}_2)\text{CH}_2\text{CH}(\text{CH}_3)_2$ ] using scanning electron microscopy (SEM). Crystallites were formed with flower-like morphologies (Fig. 4) that were distinct from the needle-like aragonite and rhombic calcite phases and were identified as vaterite using Raman microspectrometry (Thompson *et al.*, 2011). Subsequently, many different samples were produced under different growing conditions (amino acid and concentration, see Table 4). Crystals were extracted from their solutions by filtering and dried. The 12 most promising candidates were selected (using optical and electron microscopy) for the u-HT measurements. As some of the particles were large ( $\sim 20$ – $100 \mu\text{m}$ ), the precipitates were lightly ground before loading in 0.5 mm capillaries.

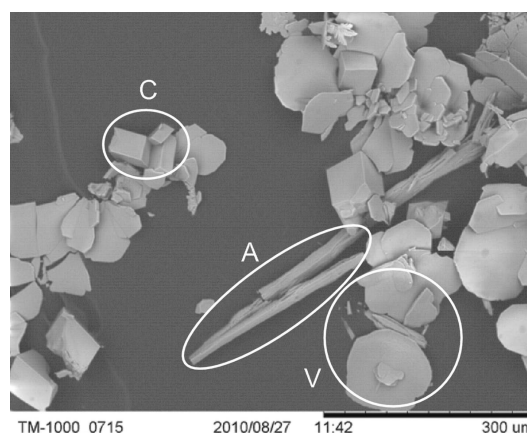


**Figure 4**  
SEM micrograph of a biomimetic  $\text{CaCO}_3$  precipitated in the presence of leucine amino acid showing the particles with various morphologies as outlined: needle aragonite (A), rhombic calcite (C), flower-like vaterite (V).

7. Results and discussion

7.1. Reference materials

Using a 15 keV X-ray beam, powder patterns were collected for the NIST SRM640c standard Si powder with acquisition times of (a) 1 s, (b) 100 ms and (c) 50 ms per frame (Fig. 5). The high (*i.e.* statistical) quality of the data enabled us to achieve good fits for each dataset using both LeBail (profile) and Rietveld (structural) refinement methods. These and subsequent patterns were least-squares fitted using the TCHZ (Thompson–Cox–Hastings) pseudo-Voigt profile and by ‘activating’ the sample displacement ( $2\theta$  corrections) and sample tilt (top hat function) facilities in *TOPAS*. The structural fits are presented in the figures. The agreement factor ( $R_{WP}$ ) obtained from the refinements for the 1 s pattern is good and is respectable for the faster patterns (Table 2). The excellent agreement between the corresponding profile (LeBail) and structural (Rietveld)  $R_{WP}$  values is particularly encouraging. The detector resolution using this diffraction geometry is essentially governed by the size of the capillary sample (0.5 mm diameter) which can be estimated using

Table 2

Agreement  $R$ -factors for profile and structural refinements of SRM640c silicon data for different collection times.

Pattern		LeBail (%)	Rietveld (%)
1 s	$R_{EXP} = 2.99$	$R_{WP} = 4.82$	$R_{WP} = 4.94$
0.1 s	$R_{EXP} = 9.18$	$R_{WP} = 11.34$	$R_{WP} = 11.37$
0.05 s	$R_{EXP} = 12.79$	$R_{WP} = 15.24$	$R_{WP} = 15.27$

equation (2) as  $\Delta 2\theta \simeq 0.04^\circ$ . The angular spread of individual peaks is very close to this as indicated by the two high-angle peaks ( $2\theta > 90^\circ$ ) plotted in Fig. 5(d), giving a good resolution of  $\Delta d/d \simeq 10^{-4}$ . At low angles ( $5^\circ \leq 2\theta \leq 40^\circ$ ) a slightly poorer result of  $\Delta d/d \simeq 10^{-3}$  was obtained.

Fig. 6(a) shows a two-dimensional plot of the phase transition of AgI from  $\beta$ - (major) and  $\gamma$ - (minor) phases to  $\alpha$ -phase. The transformation itself takes  $\sim 40$  s to complete within approximately 4 K, with the whole experiment being captured by the PSD in just over 8 min. Rietveld refinements for the datasets collected at the beginning (Fig. 6b) and end (Fig. 6c) of the transformation using the published structural parameters as starting parameters again demonstrated the

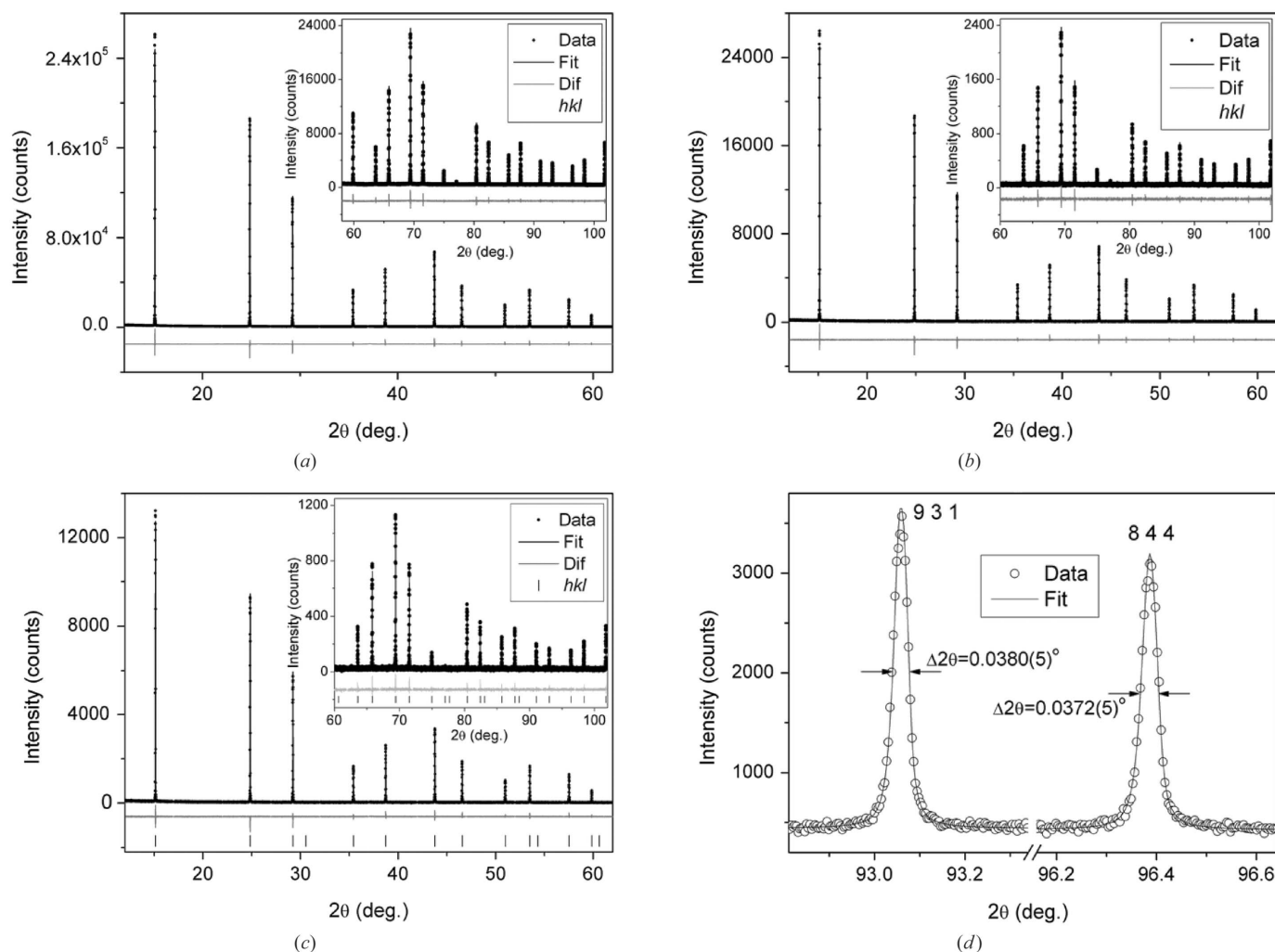
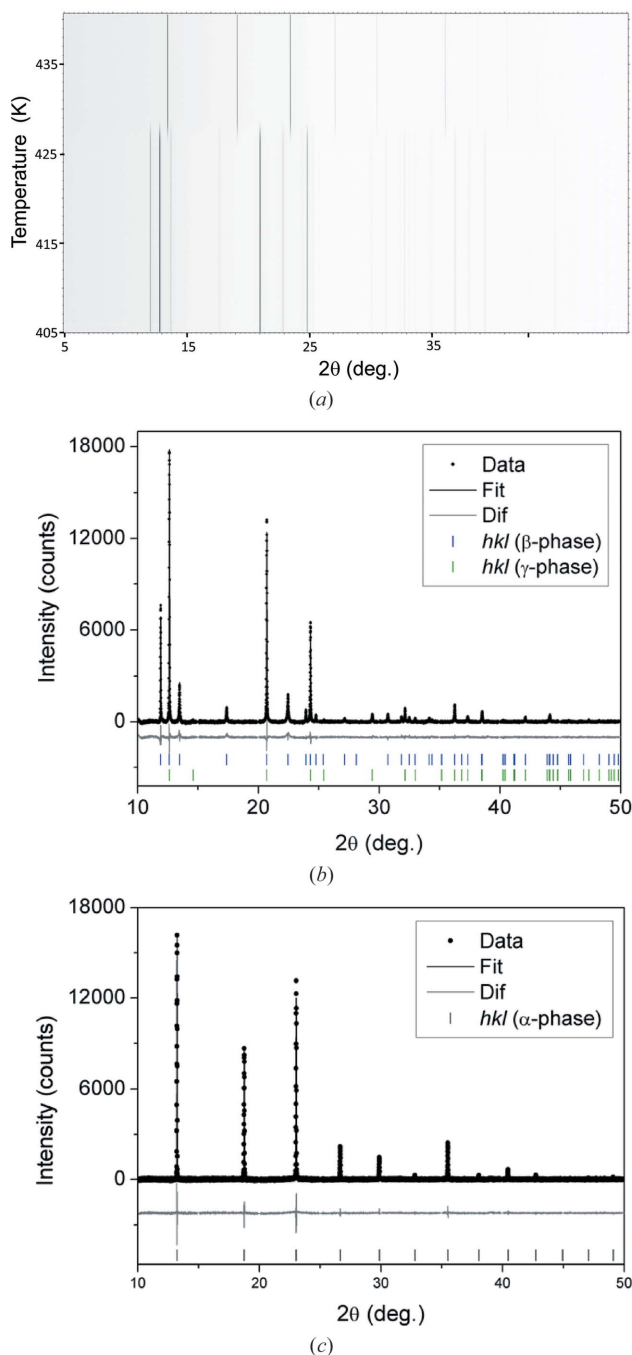


Figure 5 Diffraction patterns of Si reference powder measured using the PSD [ $\lambda = 0.826425(5) \text{ \AA}$ ] with acquisition times (a) 1 s, (b) 0.1 s and (c) 0.05 s. Each dataset is presented with the results of the final Rietveld refinement. Note that the few reflections missing were co-incident with the gaps between successive sensor modules. (d) High-angle reflections with peak widths of  $\Delta 2\theta \simeq 0.04^\circ$  showing the resolving power of the PSD.


**Figure 6**

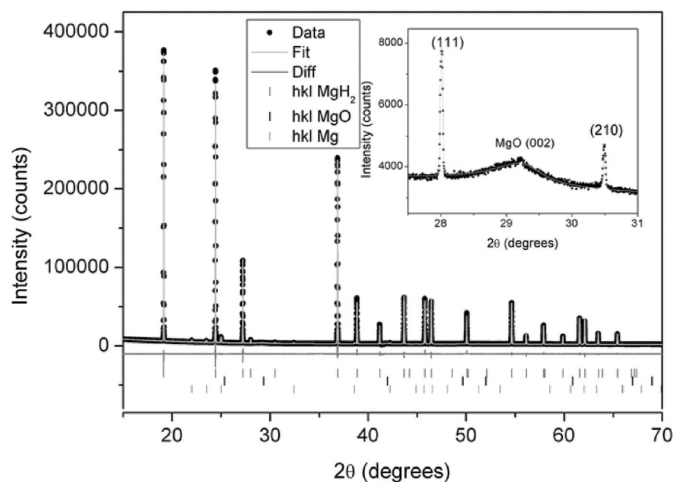
(a) A two-dimensional plot of PSD powder patterns of AgI showing the  $\beta/\gamma$ - $\alpha$  phase transition ( $\lambda = 0.825017$  Å, 1 s per pattern). Only 405–440 K temperature data are shown for clarity; note that the  $\alpha$ -phase occurs at  $\sim 428$  K. Rietveld refinements of (b) the  $\beta/\gamma$  phase at  $T = 400$  K and (c) the  $\alpha$ -phase,  $T = 450$  K.

good data quality obtained from the PSD. The final refined lattice parameters of  $a = 4.5927$  (1) and  $c = 7.5094$  (2) Å for the hexagonal structure and  $a = 6.4950$  (1) Å at  $T = 400$  K for the cubic structure were obtained with good agreement factors of  $R_{\text{EXP}} = 3.66\%$  and  $R_{\text{WP}} = 5.54\%$ . The refinement for the transformed structure produced a lattice parameter of  $a = 5.06202$  (6) Å ( $T = 450$  K) with agreement factors of  $R_{\text{EXP}} = 3.74\%$  and  $R_{\text{WP}} = 5.37\%$ .

**Table 3**

Unit-cell parameters and relative weight percent of  $\text{MgH}_2$ ,  $\text{MgO}$  and  $\text{Mg}$  phases in the sample at room temperature.

Phase	System, space group	$a$ (Å)	$c$ (Å)	wt%
$\text{MgH}_2$	Tetragonal, $P4_2/mnm$	4.51557 (1)	3.02032 (1)	90.5 (5)
$\text{MgO}$	Cubic, $Fm\bar{3}m$	4.196 (1)		7.3 (5)
$\text{Mg}$	Hexagonal, $P6_3/mmc$	3.2131 (1)	5.2156 (3)	2.2 (3)


**Figure 7**

PSD powder diffraction pattern of  $\text{MgH}_2$  at room temperature [ $\lambda = 1.062427$  (5) Å]. Cell parameters and relative weight percents of each phase ( $\text{MgH}_2$ ,  $\text{MgO}$ ,  $\text{Mg}$ ) as determined by Rietveld refinement are given in Table 3. The inset shows an enlargement of the data in the region of the  $\text{MgH}_2$  (111) and (210) reflections whose intensity arises mainly from the H-atom sub-lattice demonstrating the instrumental sensitivity.

## 7.2. Dehydrogenation of $\text{MgH}_2$

Fits to preliminary measurements at room temperature (see Fig. 7) showed that three initial phases were present in the  $\text{MgH}_2$  sample:  $\text{MgH}_2$ ,  $\text{MgO}$  and  $\text{Mg}$ . Their weight percentage (wt%) as determined by Rietveld refinements are shown in Table 3 along with their unit-cell parameters. Using *TOPAS* in batch mode, successive refinements of each collected dataset allowed the variation in wt% for each phase to be determined as a function of heating time (Fig. 8a).

The results show a gradual decrease in  $\text{MgH}_2$  with exposure time up to  $\sim 140$  frames (total time = 910 s) which is not matched by a corresponding increase in  $\text{Mg}$  but rather by an initial rise in the  $\text{MgO}$  phase (Fig. 8a, inset), which peaks at  $\sim 130$  frames (845 s) just before the main loss of hydrogen. During this dehydrogenation experiment the observed coincidence of the peak in  $\text{MgO}$  content just before the steep decline in  $\text{MgH}_2$  suggests that the  $\text{MgO}$  plays an important role in regulating the onset of hydrogen loss. While most metals have a strongly negative chemisorption enthalpy for hydrogen, almost all hydride-forming metals acquire a stable oxide skin when exposed to air, water or other oxygen atmospheres (Borgschulte *et al.*, 2008; Vigeholm *et al.*, 1980; Lei *et al.*, 2009). Friedrichs *et al.* (2006) found that nanocrystalline  $\text{MgH}_2$ , when exposed to oxygen and air, rapidly developed a 3–4 nm-thick passivation oxide layer. The  $\text{MgO}$  coating acts as a barrier to both hydrogen loss and uptake

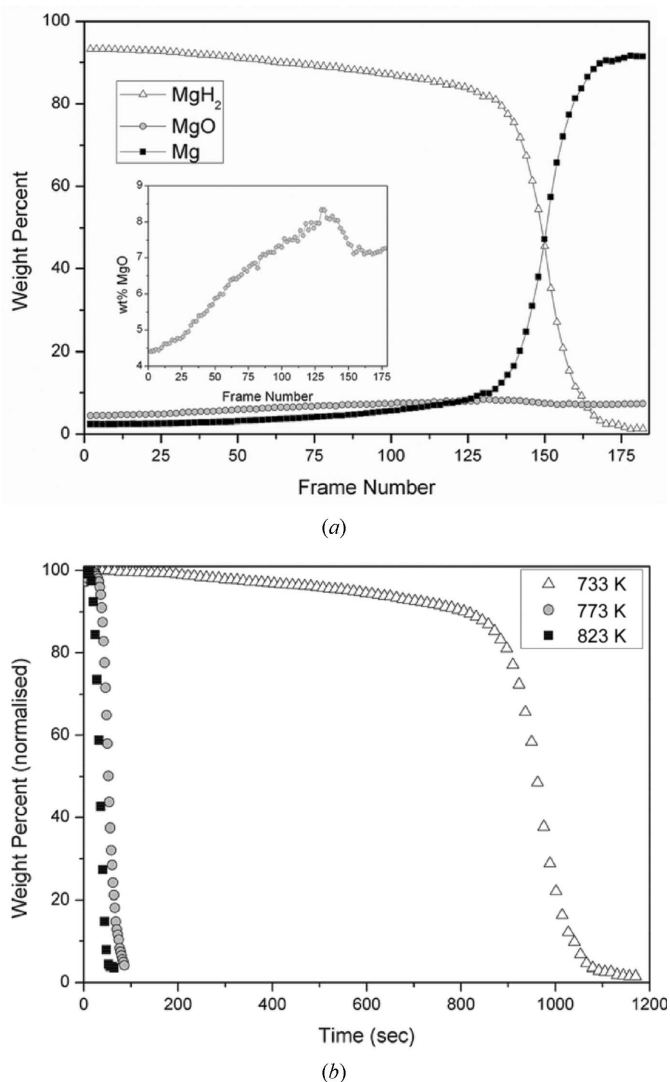


**Figure 8** (a) MgH<sub>2</sub>, Mg and MgO wt% as a function of frame number at 733 K. (b) Relative wt% of MgH<sub>2</sub> as a function of time at 733, 773 and 823 K.

from the MgH<sub>2</sub> particles, owing to its dense structure severely limiting the diffusion of H<sub>2</sub> atoms (Hjort *et al.*, 1996).

It has been reported that in order to initiate hydrogen absorption the material must thus be ‘activated’ by breaking or cracking this MgO layer, *e.g.* by using high gas pressure and/or high temperature (Lei *et al.*, 2009). The results observed here suggest the same appears to be true of hydrogen desorption. When MgO is formed at low oxygen pressure, its heat of sublimation is reduced (Wu *et al.*, 1991) and the sudden change from increasing to decreasing MgO just before dehydrogenation may be indicative of MgO loss by sublimation, which presumably would aid the cracking process. It is proposed that cracking may occur owing to a combination of the differential thermal expansion of the hydride and oxide phases, the brittle nature of the hydride phase itself (Andreassen *et al.*, 2006) and a weakening of the MgO by sublimation. The dehydrogenation was repeated at higher temperatures (Fig. 8*b*), and it can be seen that the rate of H<sub>2</sub> desorption increases with temperature. The detection sensi-

tivity and fast readout time of the I11 PSD has allowed us to capture the dehydrogenation process at much higher temporal resolution than previous experiments (*e.g.* Jensen *et al.*, 2006; Andreassen *et al.*, 2006; Riktor *et al.*, 2007) and to highlight the role that the minor oxide phase plays in the process of activation.

### 7.3. u-HT study of biomimetic vaterite

The sample change time using the I11 robotic system is 30 s (Parker *et al.*, 2011), and using a 1 s collection time for the PSD allowed a total run time for the 12 carbonate samples of ~6 min. The phases present in the precipitates and their refined lattice parameters are summarized in Table 4. We were able to determine that, within the range of concentrations used, a D-leucine concentration of between 4 and 6 g L<sup>-1</sup> produces the best vaterite crystals (samples #08 and #09). Fig. 9 shows the powder pattern for sample #09, which exhibits a strong vaterite phase mixed with aragonite and calcite (minor phase). The sharpness of the Bragg peaks for this sample (Fig. 9, inset) shows the crystalline quality of the vaterite to be good and therefore allowed the lattice parameters to be determined with high precision ( $\Delta a/a = \Delta c/c \approx 10^{-5}$ ). We used the lattice parameters of both the reduced and large hexagonal structures to fit the data and, as previously reported for vaterite derived from ikaite (Tang *et al.*, 2009), both systems gave good results. However, with agreement factors of  $R_{WP} = 5.04\%$  for the smaller cell and  $R_{WP} = 4.31\%$  for the large cell ( $R_{EXP} = 3.18\%$ ), the improvement gained by using the larger  $P6_3/mmc$  hexagonal cell is significant, strongly suggesting that the vaterite unit cell is better described by the larger structure. The results shown in Fig. 9 and the lattice parameters in Table 4 are from the final LeBail refinement using the large hexagonal cell.

This work has demonstrated that small but high-quality crystals of vaterite can be stabilized and grown *in vitro* in the presence of amino acids. Both the yield and crystal quality are dependent on the specific amino acid used in a way that has yet to be determined. However, the availability of a PSD-

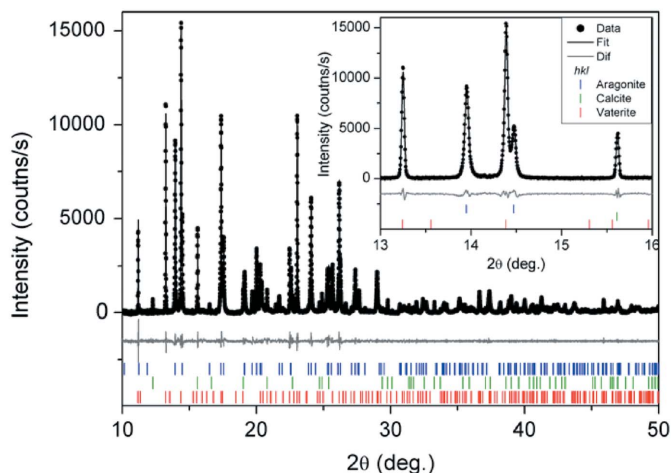


**Figure 9** Powder pattern of CaCO<sub>3</sub> precipitates formed in the presence of D-leucine (6 g L<sup>-1</sup>) showing aragonite, calcite and vaterite phases.

**Table 4**  
Crystallographic lattice parameters of CaCO<sub>3</sub> precipitated in the presence of different amino acids.

Sample	Amino acid	Amount (g)	Phase	Lattice parameters (Å)
#01	None (shaking)	–	Aragonite	$a = 4.96146$ (5), $b = 7.96963$ (8), $c = 5.74353$ (6)
			Calcite†	$a = 4.9911$ (2), $c = 17.0738$ (5)
			Vaterite†	$a = 7.1515$ (4), $c = 16.922$ (2)
#02	None (no shaking)	–	Aragonite	$a = 4.96156$ (5), $b = 7.96959$ (7), $c = 5.74365$ (6)
			Calcite†	$a = 4.99139$ (4), $c = 17.0675$ (2)
#03	L-leucine	0.1	Aragonite	$a = 4.96135$ (5), $b = 7.96996$ (8), $c = 5.74400$ (6)
			Vaterite†	$a = 7.1528$ (1), $c = 16.9329$ (3)
#04	L-leucine	0.2	Calcite†	$a = 4.99065$ (3), $c = 17.077$ (1)
			Aragonite	$a = 4.96136$ (5), $b = 7.97010$ (7), $c = 5.74410$ (5)
#05	L-leucine	0.3	Vaterite	$a = 7.1543$ (1), $c = 16.9318$ (3)
			Aragonite	$a = 4.96202$ (9), $b = 7.9721$ (1), $c = 5.7442$ (1)
#06	L-leucine	0.5	Vaterite	$a = 7.1532$ (1), $c = 16.9335$ (5)
			Aragonite	$a = 4.96217$ (7), $b = 7.9699$ (1), $c = 5.7439$ (1)
#07	D-leucine	0.1	Vaterite†	$a = 7.1521$ (1), $c = 16.9336$ (3)
			Aragonite	$a = 4.96110$ (4), $b = 7.96940$ (5), $c = 5.74370$ (5)
#08	D-leucine	0.2	Aragonite	$a = 4.96215$ (7), $b = 7.9709$ (1), $c = 5.74504$ (8)
			Calcite†	$a = 4.99109$ (7), $c = 17.0689$ (3)
			Vaterite‡	$a = 7.15352$ (7), $c = 16.9337$ (2)
#09	D-leucine	0.3	Aragonite	$a = 4.96208$ (8), $b = 7.9690$ (1), $c = 5.7443$ (1)
			Calcite†	$a = 4.9912$ (1), $c = 17.0689$ (5)
			Vaterite‡	$a = 7.15322$ (9), $c = 16.9329$ (2)
#10	L-alanine	0.5	Aragonite	$a = 4.9618$ (2), $b = 7.9713$ (3), $c = 5.7431$ (2)
			Calcite†	$a = 4.99173$ (6), $c = 17.0682$ (3)
#11	D-alanine	0.5	Aragonite	$a = 4.96156$ (5), $b = 7.96959$ (7), $c = 5.74365$ (6)
			Calcite	$a = 4.9917$ (1), $c = 17.0710$ (6)
			Vaterite	$a = 7.1552$ (1), $c = 16.9381$ (4)
#12	L-glutamide	0.5	Calcite	$a = 4.9937$ (1), $c = 17.0665$ (5)

† Weak phase. ‡ Strong phase.

based u-HT facility allows the outcome of multiple synthesis experiments to be assessed quickly. The outcome of this u-HT work has formed the basis for further experiments on this rare calcium carbonate phase, including a detailed structural study using the small-molecule (micro-single-crystal) diffraction facility (beamline I19) at Diamond to confirm the assignment of the space group and the investigation of its thermal expansion and phase transformation using I11. The results of these investigations will be reported in the future.

## 8. Conclusions

We have described the commissioning of a PSD device for fast powder diffraction studies on beamline I11 at Diamond Light Source. Results obtained for a certified Si reference sample demonstrate that the data quality is suitable for structural refinement, even for powder patterns collected in sub-second time frames. Although the resolution is governed by the sample size ( $\Delta d/d \simeq 10^{-3}$ – $10^{-4}$  for a 0.5 mm capillary sample), the speed of data collection is much faster compared with conventional  $2\theta$  scanning. The  $\beta/\gamma$ - $\alpha$  phase transition of silver iodide was ‘captured’ in a few tens of seconds, while time-resolved measurements of the potential hydrogen storage material MgH<sub>2</sub> and ultrafast high-throughput measurements of biomimetic carbonates further demonstrated the capability of the PSD for scientific applications. Now in full user operation, the PSD is routinely employed in a wide range of scientific applications. Clarke *et al.* (2011) have used the PSD to study weakly diffracting systems such as hydrocarbon

monolayers adsorbed on a graphite substrate. Another growing area of application among the I11 user community is in the study of materials that suffer radiation damage when exposed to the intense X-ray beam. Here, the PSD has been used to both capture the initial structure well before the onset of structural degradation and monitor that process as it occurs (Vitorica-Yrezabel *et al.*, 2011). In conclusion, the successful installation and commissioning of the PSD facility for fast powder diffraction has expanded the range and type of scientific experiments that can now be performed on I11, in addition to the types of materials that can be studied by powder diffraction, significantly enhancing the beamline’s capability.

We would like to express our thanks to Bernd Schmitt and Anna Bergamaschi of the Paul Scherrer Institute, Switzerland, for their technical assistance and advice during the commissioning of the PSD.

## References

- Aizenberg, J., Lambert, G., Addadi, L. & Weiner, S. (1996). *Adv. Mater.* **8**, 222–226.
- Aizenberg, J., Lambert, G., Weiner, S. & Addadi, L. (2002). *J. Am. Chem.* **124**, 32–39.
- Andreasen, A., Sørensen, M. B., Burkarl, R., Møller, B., Molenbroek, A. M., Pedersen, A. S., Vegge, T. & Jensen, T. R. (2006). *Appl. Phys. A*, **82**, 515–521.
- Barber, D. J. (1994). *Scr. Metall. Mater.* **31**, 989–994.
- Bergamaschi, A., Broennimann, ch., Dinapoli, R., Eikenberry, E., Gozzo, F., Henrich, B., Kobas, M., Kraft, P., Patterson, B. & Schmitt, B. (2008). *Nucl. Instrum. Methods Phys. Res. A*, **591**, 163–166.
- Bergamaschi, A., Cervellino, A., Dinapoli, R., Gozzo, F., Henrich, B., Johnson, I., Kraft, P., Mozzanica, A., Schmitt, B. & Shi, X. (2009). *Nucl. Instrum. Methods Phys. Res. A*, **604**, 136–139.
- Bergamaschi, A., Cervellino, A., Dinapoli, R., Gozzo, F., Henrich, B., Johnson, I., Kraft, P., Mozzanica, A., Schmitt, B. & Shi, X. (2010). *J. Synchrotron Rad.* **17**, 653–668.
- Bezares, J., Asaro, R. J. & Hawley, M. (2008). *J. Struct. Biol.* **163**, 61–75.
- Borgschulte, A., Biemann, M., Zuttel, A., Barkhordarian, G., Dornheim, M. & Bormann, R. (2008). *Appl. Surf. Sci.* **254**, 2377–2384.
- Cernik, R. J., Barnes, P., Bushnell-Wye, G., Dent, A. J., Diakun, G. P., Flaherty, J. V., Greaves, G. N., Heeley, E. L., Hellsby, W., Jacques, S. D. M., Kay, J., Rayment, T., Ryan, A., Tang, C. C. & Terrill, N. J. (2004). *J. Synchrotron Rad.* **11**, 163–170.
- Cernik, R. J., Murray, P. K., Pattison, P. & Fitch, A. N. (1990). *J. Appl. Cryst.* **23**, 292–296.
- Cheary, R. W. & Coelho, A. A. (1998a). *J. Appl. Cryst.* **31**, 851–861.
- Cheary, R. W. & Coelho, A. A. (1998b). *J. Appl. Cryst.* **31**, 862–868.

- Checa, A. G., Saánchez-Navas, A. & Rodríguez-Navarro, A. (2009). *Cryst. Growth Des.* **9**, 4574–4580.
- Clarke, S. M., Frišćić, T., Jones, W., Mandal, A., Sun, C. & Parker, J. E. (2011). *Chem. Commun.* **47**, 2526–2528.
- Cox, D. E., Hastings, J. B., Thomlinson, W. & Prewitt, C. T. (1983). *Nucl. Instrum. Methods*, **208**, 573–578.
- Finger, L. W., Cox, D. E. & Jephcoat, A. P. (1994). *J. Appl. Cryst.* **27**, 892–900.
- Fitch, A. N. (1996). *Mater. Sci. Forum*, **228–231**, 219.
- Fitch, A. N. (2004). *J. Res. Natl. Inst. Stand. Technol.* **109**, 133–142.
- Friedrichs, O., Sánchez-López, J. C., López-Cartes, C., Dornheim, M., Klassen, T., Bormann, R. & Fernández, A. (2006). *Appl. Surf. Sci.* **252**, 2334–2345.
- Gozzo, F., Cevellino, A., Leoni, M., Scarli, P., Bergamaschi, A. & Schmitt, B. (2010). *Z. Kristallogr.* **225**, 616–624.
- Gozzo, F., Schmitt, B., Bortolamedi, Th., Giannini, C., Guagliardi, A., Lange, M., Meister, D., Maden, D., Willmott, P. & Patterson, B. D. (2004). *J. Alloys Compd.* **362**, 206–217.
- Hasegawa, K., Mochiki, K., Koine, M., Satow, Y., Hashizume, H. & Iitake, Y. (1986). *Nucl. Instrum. Methods Phys. Res. A*, **252**, 158–168.
- Hastings, J. B., Thomlinson, W. & Cox, D. E. (1984). *J. Appl. Cryst.* **17**, 85–95.
- Haverkamp, R. G. & Wallwork, K. S. (2009). *J. Synchrotron Rad.* **16**, 849–856.
- Hjort, P., Krozer, A. & Kasemo, B. (1996). *J. Alloys Compd.* **237**, 74–80.
- Hodeau, J. L., Bordet, P., Anne, M., Prat, A., Fitch, A. N., Dooryhée, E., Vaughan, G. & Freund, A. (1998). *Proc. SPIE*, **3448**, 353–361.
- Jacob, D. E., Soldati, A. L., Wirth, R., Huth, J., Wehrmeister, U. & Hofmeister, W. (2008). *Geochim. Cosmochim. Acta*, **72**, 5401–5415.
- Jensen, T. R., Andreasen, A., Vegge, T., Andreasen, J. W., Ståhl, K., Pedersen, A. S., Nielsen, M. M., Molenbroek, A. M. & Besenbacher, F. (2006). *Int. J. Hydrogen Energy*, **31**, 2052–2062.
- Kamhi, S. R. (1963). *Acta Cryst.* **16**, 770–772.
- Kvick, A. (2003). *Nucl. Instrum. Methods Phys. Res. B*, **199**, 531–535.
- Lee, P. L., Shu, D., Ramanathan, M., Preissner, C., Wang, J., Beno, M. A., Von Dreele, R. B., Ribaud, L., Kurtz, C., Antao, S. M., Jiao, X. & Toby, B. H. (2008). *J. Synchrotron Rad.* **15**, 427–432.
- Lei, J. P., Huang, H., Dong, X. L., Sun, J. P., Lu, B., Lei, M. K., Wang, Q., Dong, C. & Cao, G. Z. (2009). *Int. J. Hydrogen Energy*, **34**, 8127–8134.
- Lennie, A. R., Laundry, D., Roberts, M. A. & Bushnell-Wye, G. (2007). *J. Synchrotron Rad.* **14**, 433–438.
- Lowenstam, H. A. & Abbott, D. P. (1975). *Science*, **188**, 363–365.
- Marchal, J. (2010a). *J. Instrum.* **5**, P11002.
- Marchal, J. (2010b). *J. Instrum.* **5**, P01004.
- Martorana, A., Deganello, G., Longo, A., Deganello, F., Liotta, L., Macaluso, A., Pantaleo, G., Balerna, A., Meneghini, C. & Mobilio, S. (2003). *J. Synchrotron Rad.* **10**, 177–182.
- Mellander, B.-E., Bowling, J. E. & Baranowski, B. (1980). *Phys. Scr.* **22**, 541–544.
- Merrill, L. (1977). *J. Phys. Chem. Ref. Data*, **6**, 1205.
- Meyer, H.-J. (1960). *Fortschr. Mineral.* **38**, 186–187.
- Meyer, H.-J. (1969). *Z. Kristallogr.* **128**, 183–212.
- Mikkelsen, A., Engelsen, S. B., Hansen, H. C. B., Larsen, O. & Skibsted, L. H. (1997). *J. Cryst. Growth*, **177**, 125–134.
- Nishibori, E., Takata, M., Kato, K., Sakata, M., Kubota, Y., Aoyagi, S., Kuroiwa, Y., Yamakata, M. & Ikeda, N. (2001). *Nucl. Instrum. Methods Phys. Res. A*, **467–468**, 1045–1048.
- Norby, P. (1997). *J. Appl. Cryst.* **30**, 21–30.
- Parker, J. E., Thompson, S. P., Cobb, T. M., Yuan, F., Potter, J., Lennie, A. R., Alexander, S., Tighe, C. J., Darr, J. A., Cockcroft, J. C. & Tang, C. C. (2011). *J. Appl. Cryst.* **44**, 102–110.
- Parker, J. E., Thompson, S. P., Lennie, A. R. & Tang, C. C. (2010). *CrystEngComm*, **12**, 1590–1599.
- Riktor, M. D., Sørby, M. H., Chłopek, K., Fichtner, M., Buchter, F. A., Züttel, A. & Hauback, B. C. (2007). *J. Mater. Chem.* **17**, 4939–4942.
- Schlapbach, L. & Züttel, A. (2001). *Nature (London)*, **414**, 353–358.
- Schmitt, B., Brönnimann, ch., Eikenberry, E. F., Gozzo, F., Hörmann, C., Horisberger, R. & Patterson, B. (2003). *Nucl. Instrum. Methods Phys. Res. A*, **501**, 267–272.
- Smith, G. C. (1991). *Synchrotron Radiat. News*, **3**, 23.
- Spann, N., Harper, E. M. & Aldridge, D. C. (2010). *Naturwissenschaften*, **97**, 743–751.
- Svensson, S. O., Birch, J., Müller, H. & Kvick, Å. (1997). *J. Synchrotron Rad.* **4**, 83–94.
- Tang, C. C., Martin, C. M., Laundry, D., Thompson, S. P., Diakun, G. P. & Cernik, R. J. (2004). *Nucl. Instrum. Methods Phys. Res. B*, **222**, 659–666.
- Tang, C. C., Thompson, S. P., Hill, T. P., Wilkin, G. R. & Wagner, U. H. (2007). *Z. Kristallogr.* **26**, 153.
- Tang, C. C., Thompson, S. P., Parker, J. E., Lennie, A. R., Azough, F. & Kato, K. (2009). *J. Appl. Cryst.* **42**, 225–233.
- Thompson, S. P., Parker, J. E., Potter, J., Hill, T. P., Birt, A., Cobb, T. M., Yuan, F. & Tang, C. C. (2009). *Rev. Sci. Instrum.* **80**, 075107.
- Thompson, S. P., Parker, J. E., Street, S. R. & Tang, C. C. (2011). *J. Phys. Conf. Ser.* **286**, 012030.
- Toraya, H., Hibino, H. & Ohsumi, K. (1996). *J. Synchrotron Rad.* **3**, 75–83.
- Vigeholm, B., Kjoller, J. & Larsen, B. (1980). *J. Less-Common Metals*, **74**, 341–350.
- Vitorica-Yrezabel, I. J., Sullivan, R. A., Purver, S. L., Curfs, C., Tang, C. C. & Brammer, L. (2011). *CrystEngComm*, **13**, 3189–3196.
- Wallwork, K. S., Kennedy, B. J. & Wang, D. (2007). *AIP Conf. Proc.* **879**, 879–882.
- Wang, L., Sondi, I. & Matijevic, E. (1999). *J. Colloid Interface Sci.* **218**, 545–553.
- Wang, J., Toby, B. H., Lee, P. L., Ribaud, L., Antao, S. M., Kurtz, C., Ramanathan, M., Von Dreele, R. B. & Beno, M. A. (2008). *Rev. Sci. Instrum.* **79**, 085105.
- Wu, M.-C., Corneille, J. S., Estrada, C. A., He, J.-W. & Goodman, D. W. (1991). *Chem. Phys. Lett.* **182**, 472.
- Zachariasen, W. H., Holley, C. E. & Stamper, J. F. (1963). *Acta Cryst.* **16**, 352–353.